Supporting Information

In-situ coating N, S-codoped porous carbon thin film on carbon nanotubes as an advanced metal-free bifunctional oxygen electrocatalyst for Zn-air batteries

Xin Wang,[a] Guang-Lan Li,[a*] Shuo Cao,[a] Zhong-Fa Lu,[a] Ce Hao,[a] Suli Wang,[b] Gongquan Sun[b]

[a] *State Key Laboratory of Fine Chemicals, Dalian University of Technology, Dalian 116023, PR China. School of Chemical Engineering, Dalian University of Technology, Panjin 124221, PR China.*

[b] *Division of Fuel Cells and Battery, Dalian National Laboratory for Clean Energy, Dalian Institute of Chemical Physics, Chinese Academy of Sciences, Dalian 116023, China; Key Laboratory of Fuel Cells & Hybrid Power Sources, Chinese Academy of Sciences, Dalian 116023, China.*

*Corresponding authors. E-mail addresses: guanglanli@dlut.edu.cn (G.-L. Li)

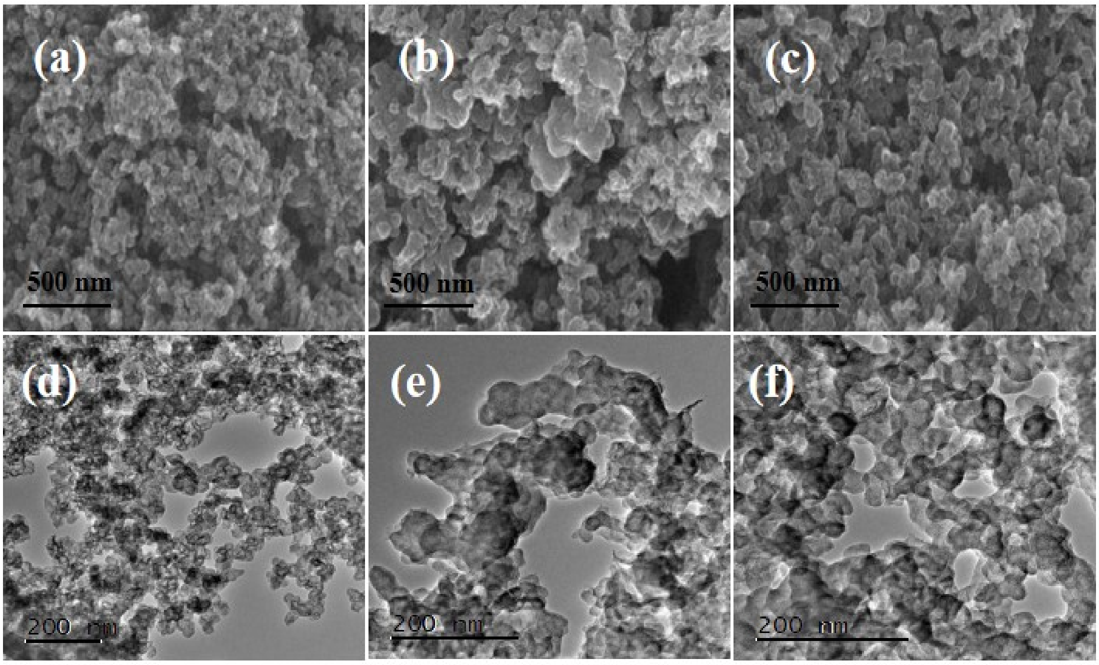

Figure S1. SEM images of (a) KB@NSCF, (b) VXC@NSCF, and (c) AC@NSCF catalysts; TEM images of (d) KB@NSCF, (e) VXC@NSCF, and (f) AC@NSCF catalysts.

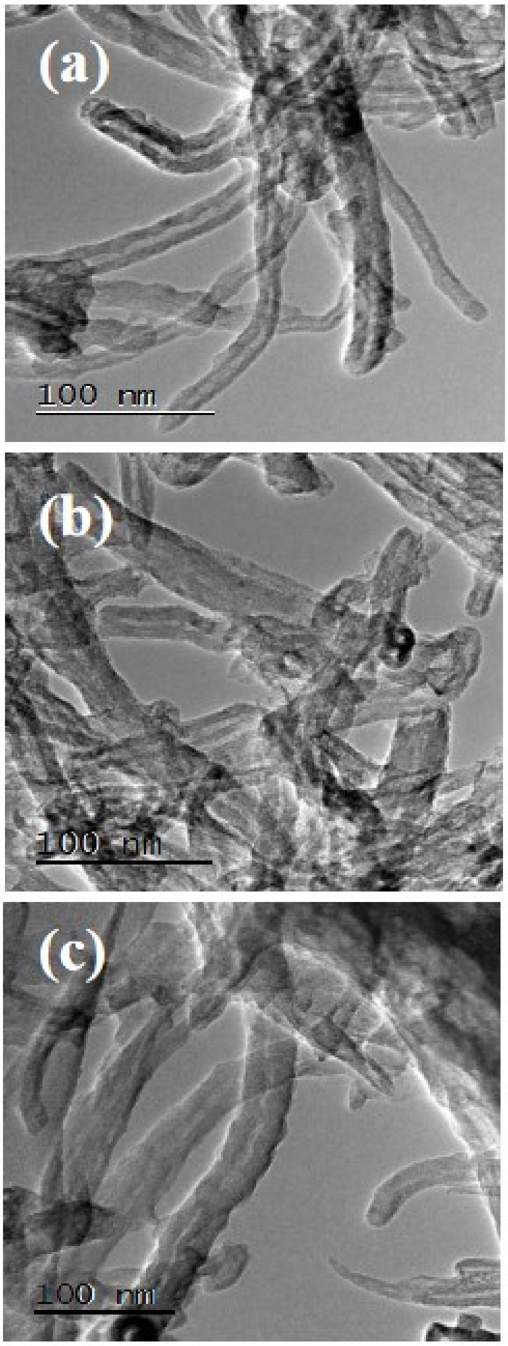

Figure S2. TEM images of (a) CNT@NSCF$_0$, (b) NCF@CNT, and (c) CNT@NSCF.

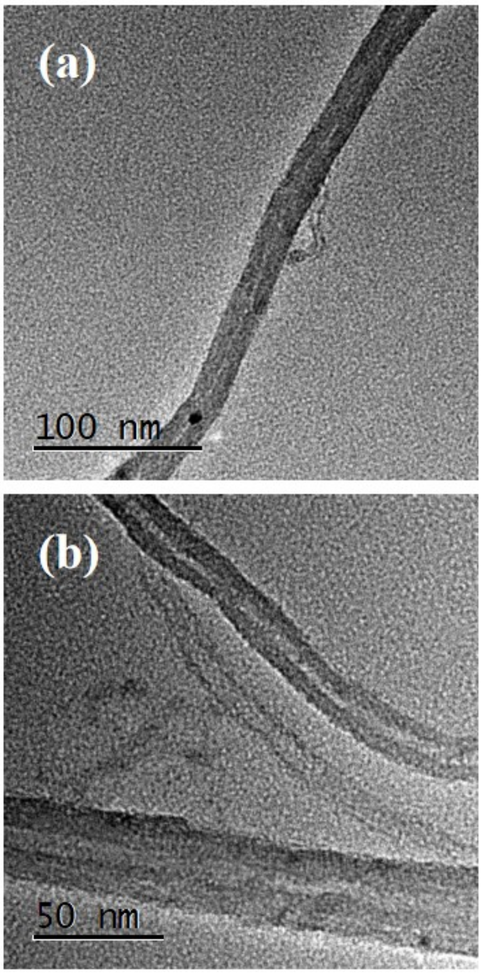

Figure S3. TEM images of CNT.

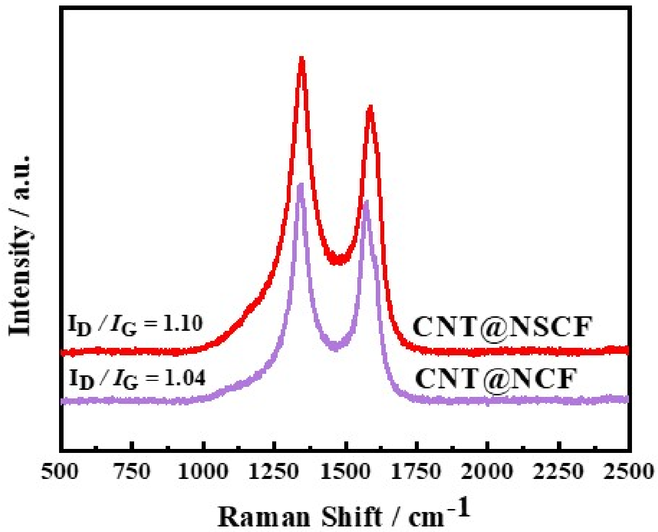

Figure S4. Raman spectra of CNT@NSCF and CNT@NCF catalysts.

Table S1 The parameters of porous structures based on BET data for the prepared samples.

Samples	Specific surface area (m^2 g^{-1})	Total pore volume (cm^3 g^{-1})	Average pore diameter (nm)
CNT@NSCF	748.4	1.45	4.78
KB@NSCF	949.7	1.84	5.91
VXC@NSCF	553.3	0.994	4.25
AC@NSCF	525.8	0.899	4.18

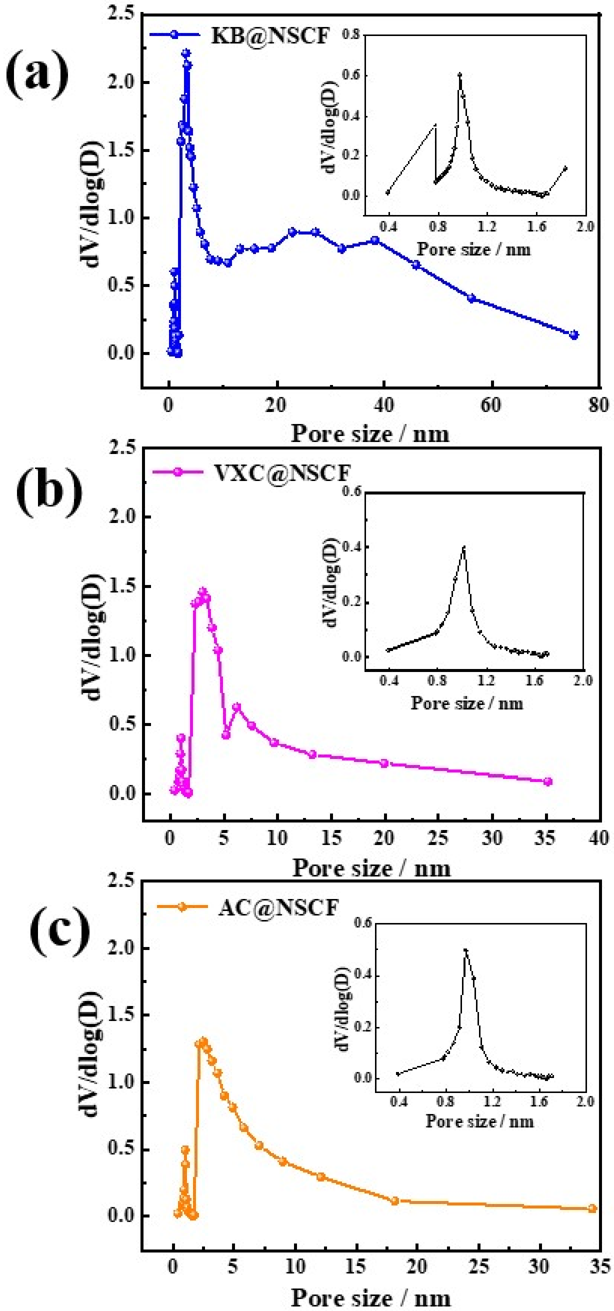

Figure S5. The pore distribution curves of KB@NSCF, VXC@NSCF, and AC@NSCF catalysts. Insets: enlarged views of the corresponding micropore distribution curves.

Table S2 Element contents (at. %) of CNT, KB, VXC, and AC derived from XPS.

Element	CNT	KB	VXC	AC
C (at. %)	91.75	99.11	98.28	99.02
O (at. %)	8.25	0.89	1.72	0.98

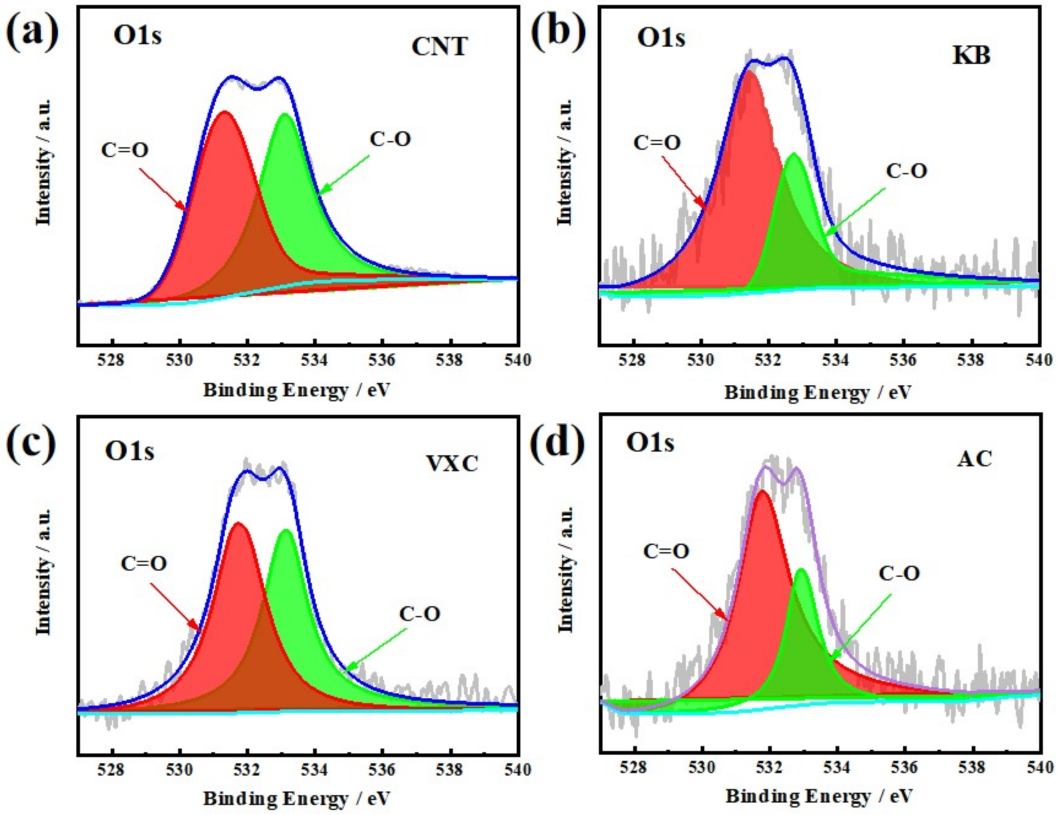

Figure S6. High resolution O 1s XPS spectra of (a) CNT; (b) KB; (c) VXC; and (d) AC.

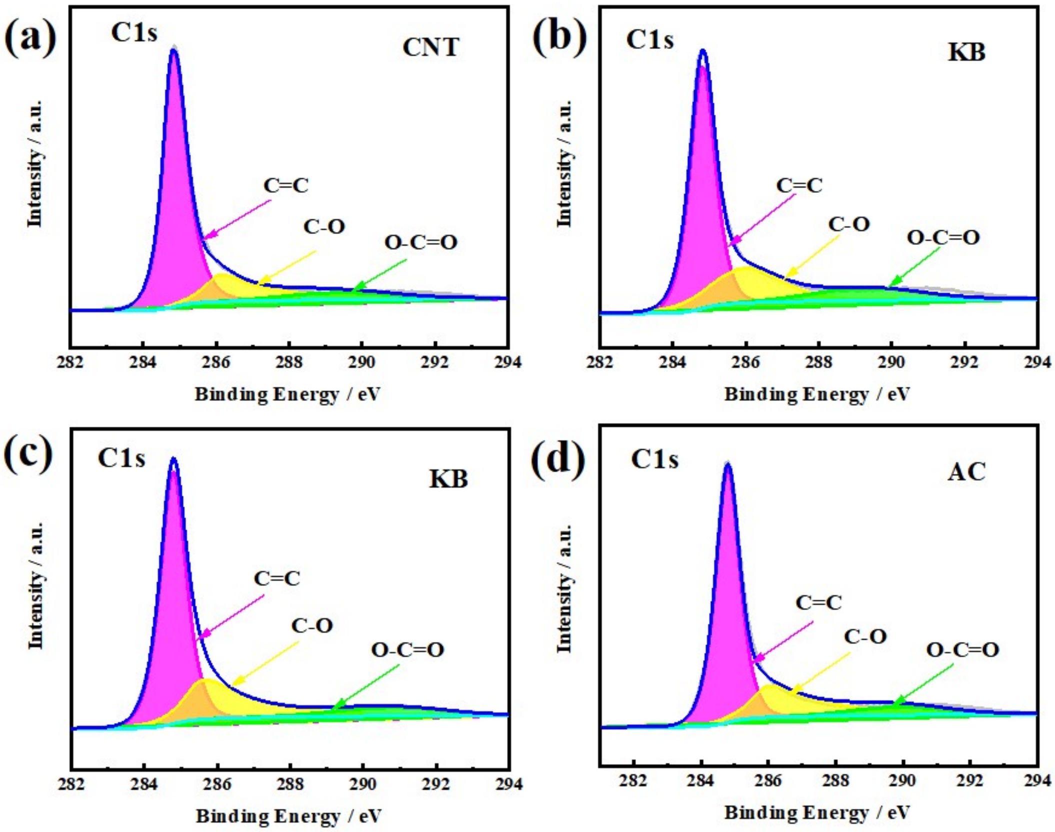

Figure S7. High resolution C1s XPS spectra of (a) CNT; (b) KB; (c) VXC; and (d) AC.

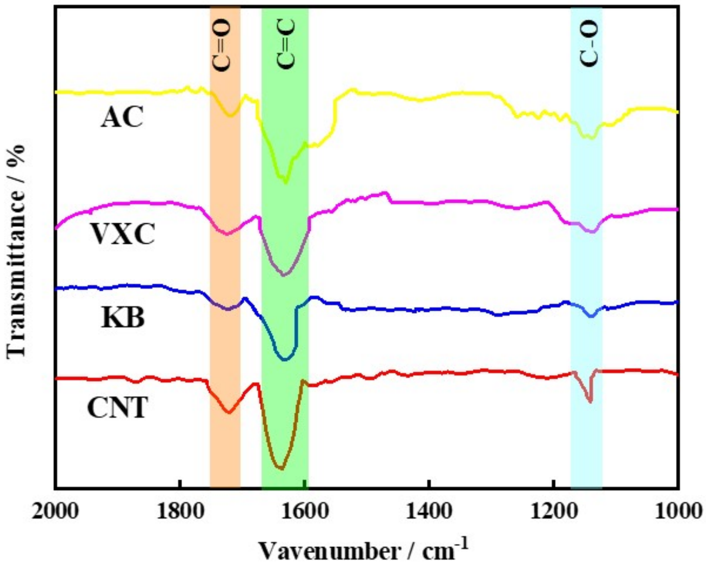

Figure S8. FTIR spectra of CNT, KB, VXC and AC.

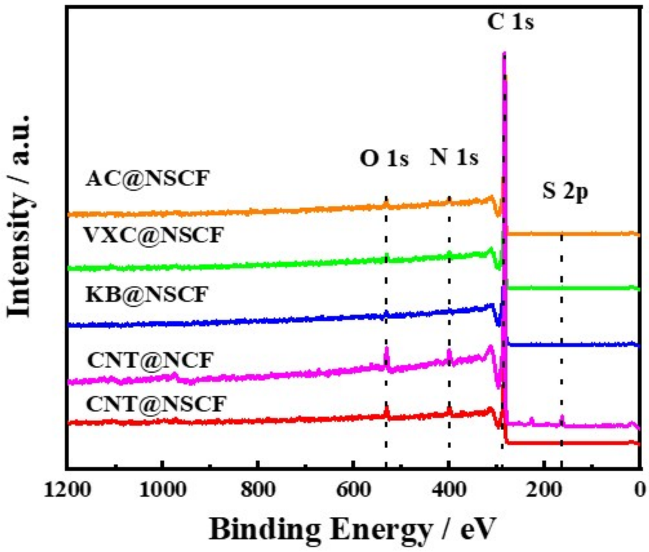

Figure S9. XPS spectra of CNT@NSCF, KB@NSCF, VXC@NSCF, and AC@NSCF.

Table S3. The element contents (at. %) of N, S, C, and O based on the XPS.

Element	CNT@NSCF	$CNT@NSCF_0$	KB@NSCF	VXC@NSCF	AC@NSCF	CNT@NCF
O (at. %)	3.81	6.57	1.17	1.99	2.23	3.19
C (at. %)	90.63	84.56	94.61	94.57	94.63	91.75
S (at. %)	0.38	0.90	0.27	0.37	0.31	/
N (at. %)	5.18	7.98	3.95	3.07	2.83	5.06
N+S (at. %)	5.56	8.88	4.22	3.44	3.14	/

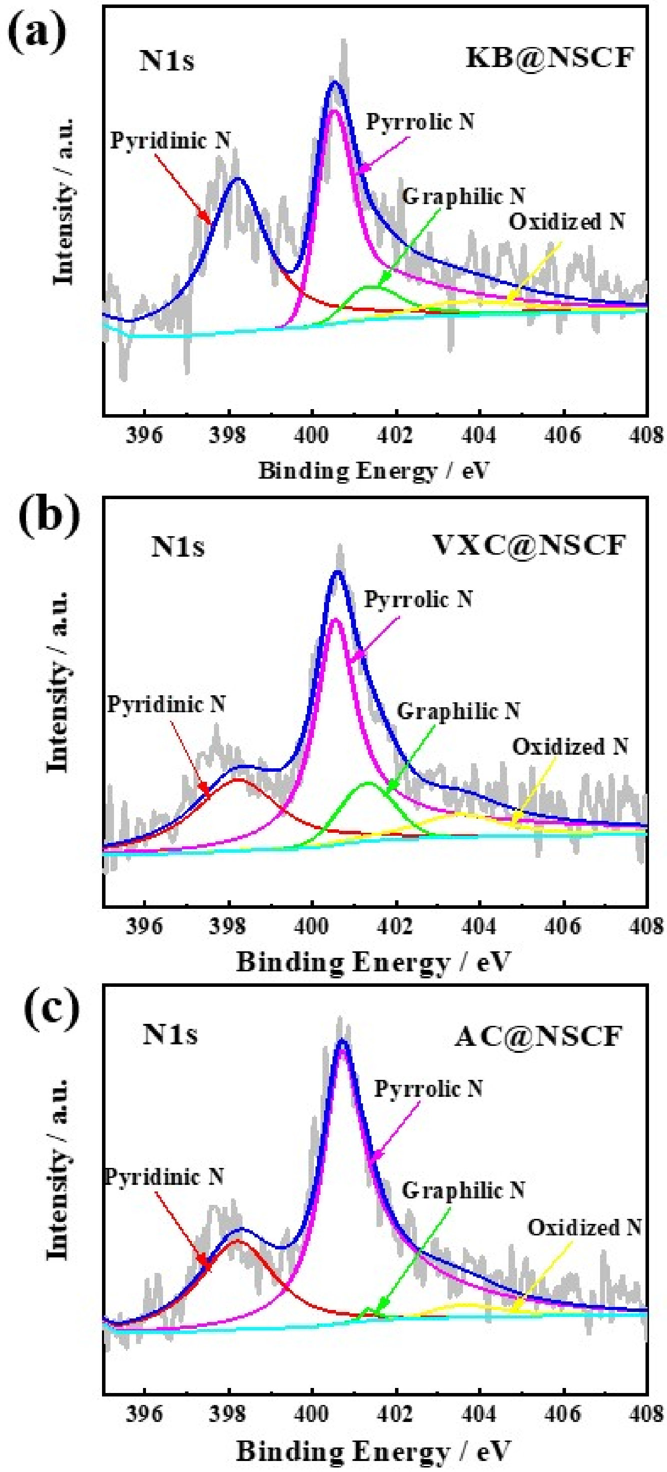

Figure S10. High resolution N1s XPS spectra of (a) KB@NSCF, (b) VXC@NSCF, and (c) AC@NSCF.

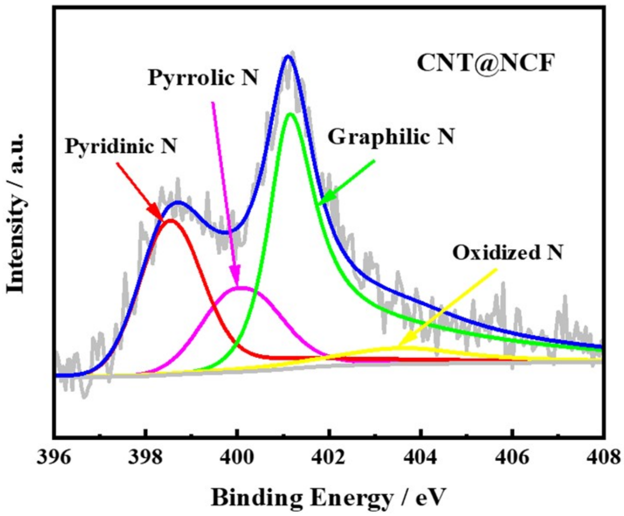

Figure S11. High resolution N 1s XPS spectrum of CNT@NCF.

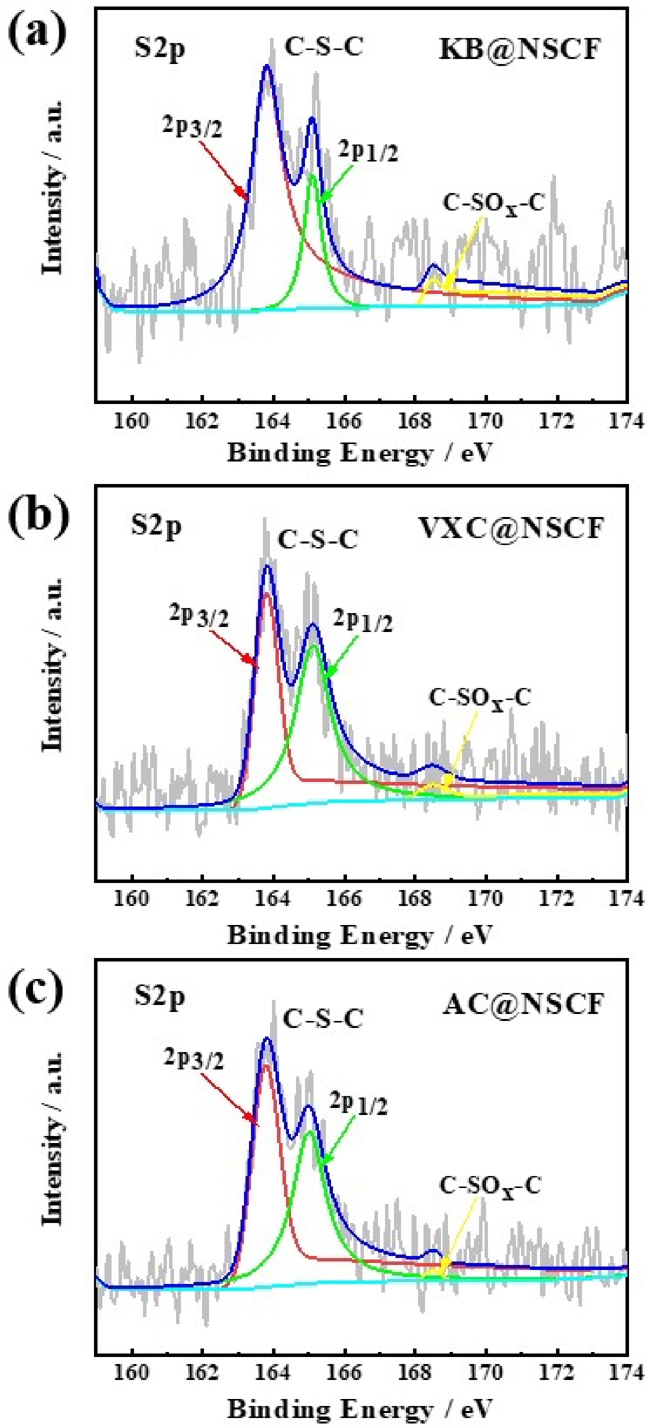

Figure S12. High resolution S 2p XPS spectra of (a) KB@NSCF, (b) VXC@NSCF, and (c) AC@NSCF.

Table S4 The percentage of N species and S species derived from high-resolution N 1s and S 2p spectra of catalysts.

Species	CNT@NSCF	CNT@NSCF$_0$	KB@NSCF	VXC@NSCF	AC@NSCF	CNT@NCF
Graphitic N (%)	14.75	/	11.41	10.87	7.89	50.02
Pyridinic N (%)	55.46	82.22	35.7	23.4	20.14	20.88
Pyrrolic N (%)	25.48	17.78	41.02	55.84	60.95	16.88
Oxidic N (%)	4.31	/	11.87	9.89	11.02	12.22
thiophene S (%)	98.36	28.18	93.23	94.61	97.65	/
Oxidic S (%)	1.64	71.82	6.77	5.39	2.35	/

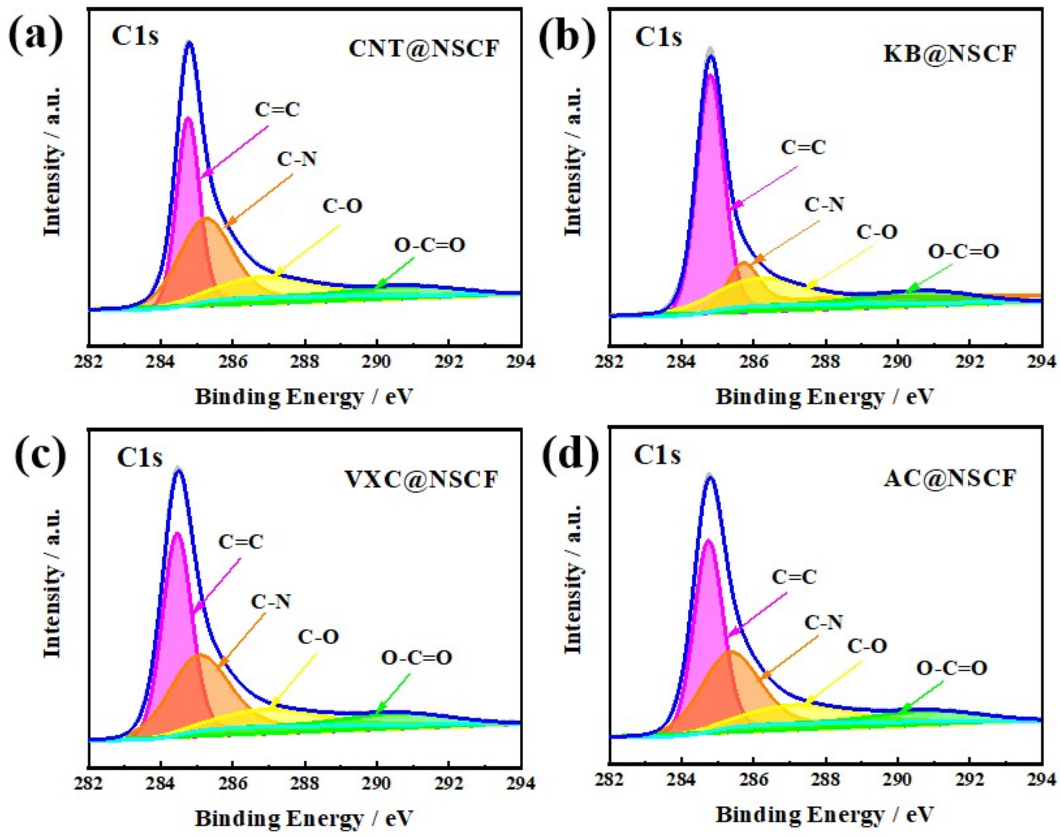

Figure S13. High resolution C1s XPS spectra of (a) CNT@NSCF, (b) KB@NSCF, (c) VXC@NSCF, and (d) AC@NSCF.

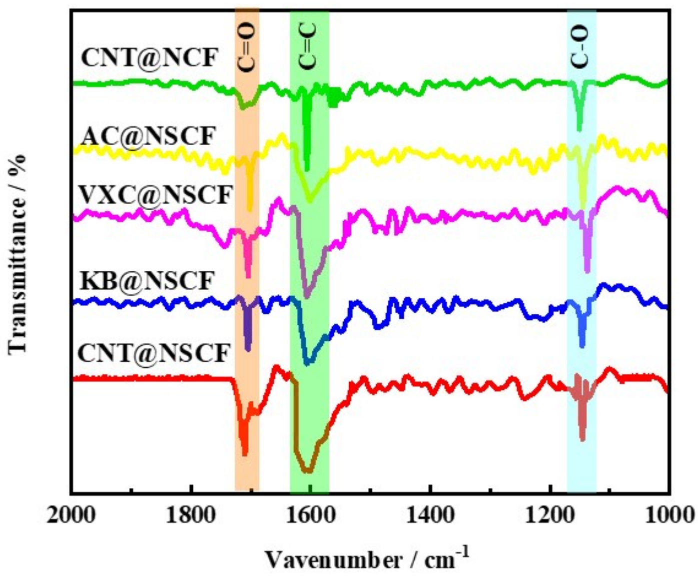

Figure S14. FTIR spectra of CNT@NSCF, KB@NSCF, VXC@NSCF, AC@NSCF and CNT@NCF.

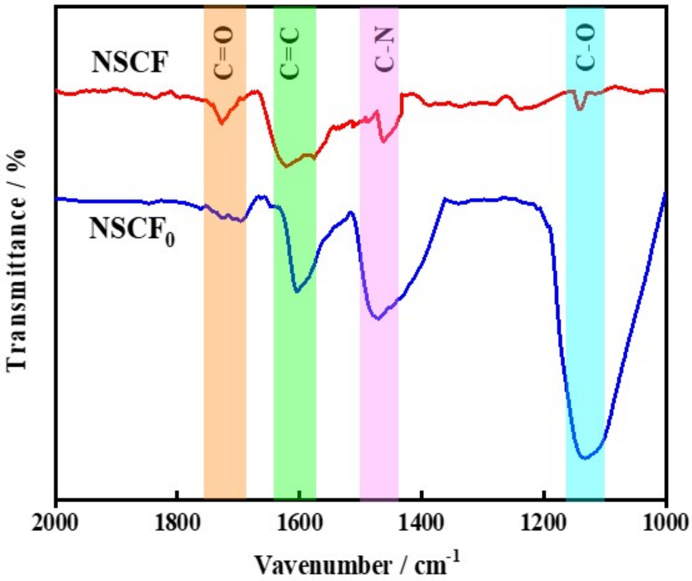

Figure S15. FTIR spectra of $NSCF_0$ and NSCF.

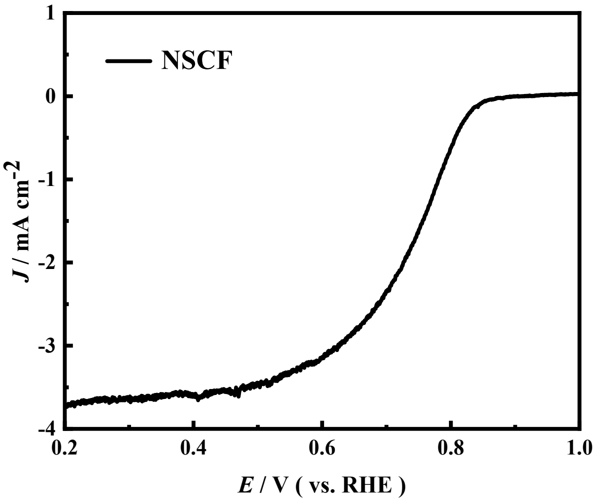

Figure S16. ORR LSV curves of NSCF recorded at 1600 rpm and 10 mV s^{-1}.

Table S5 The ORR onset potential, half-wave potential and limiting current density of CNT@NSCF, KB@NSCF, VXC@NSCF, AC@NSCF, and Pt/C in 0.1 M KOH.

	CNT@NSCF	KB@NSCF	VXC@NSCF	AC@NSCF	NSCF	Pt/C
E_{onset} / V	0.94	0.90	0.88	0.89	0.84	0.97
$E_{1/2}$ / V	0.82	0.79	0.77	0.79	0.73	0.84
j_{lim} / mA cm^{-2}	5.98	5.72	5.14	3.62	3.73	4.98

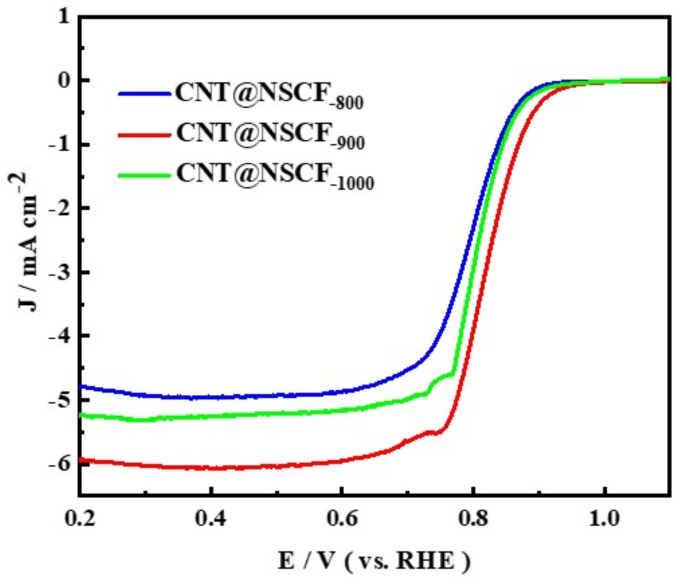

Figure S17. ORR LSV curves of CNT@NSCF at different temperature recorded at 1600 rpm and 10 mV s^{-1}.

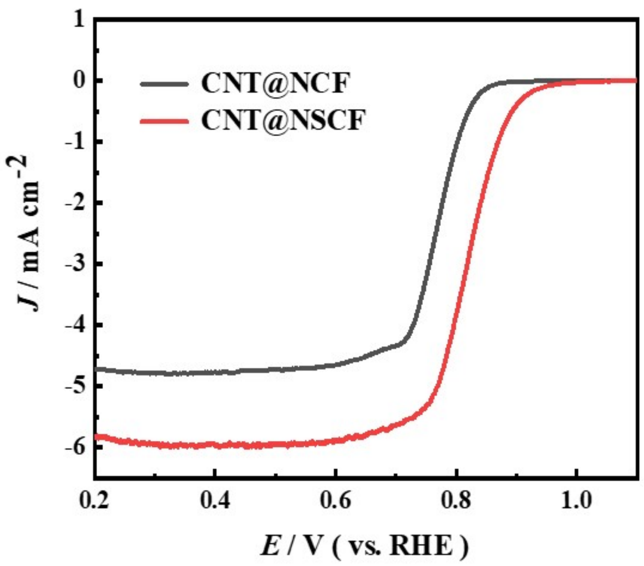

Figure S18. ORR LSV curves of CNT@NSCF and CNT@NCF recorded at 1600 rpm and 10 mV s^{-1}.

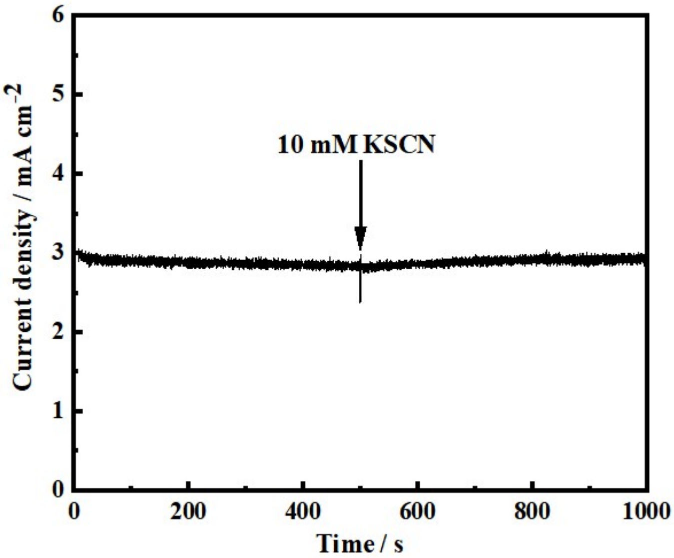

Figure S19. Chronoamperometric response of CNT@NSCF in O_2-saturated 0.10 M KOH with the addition of KSCN (resulting in an electrolyte with 0.01 M KSCN).

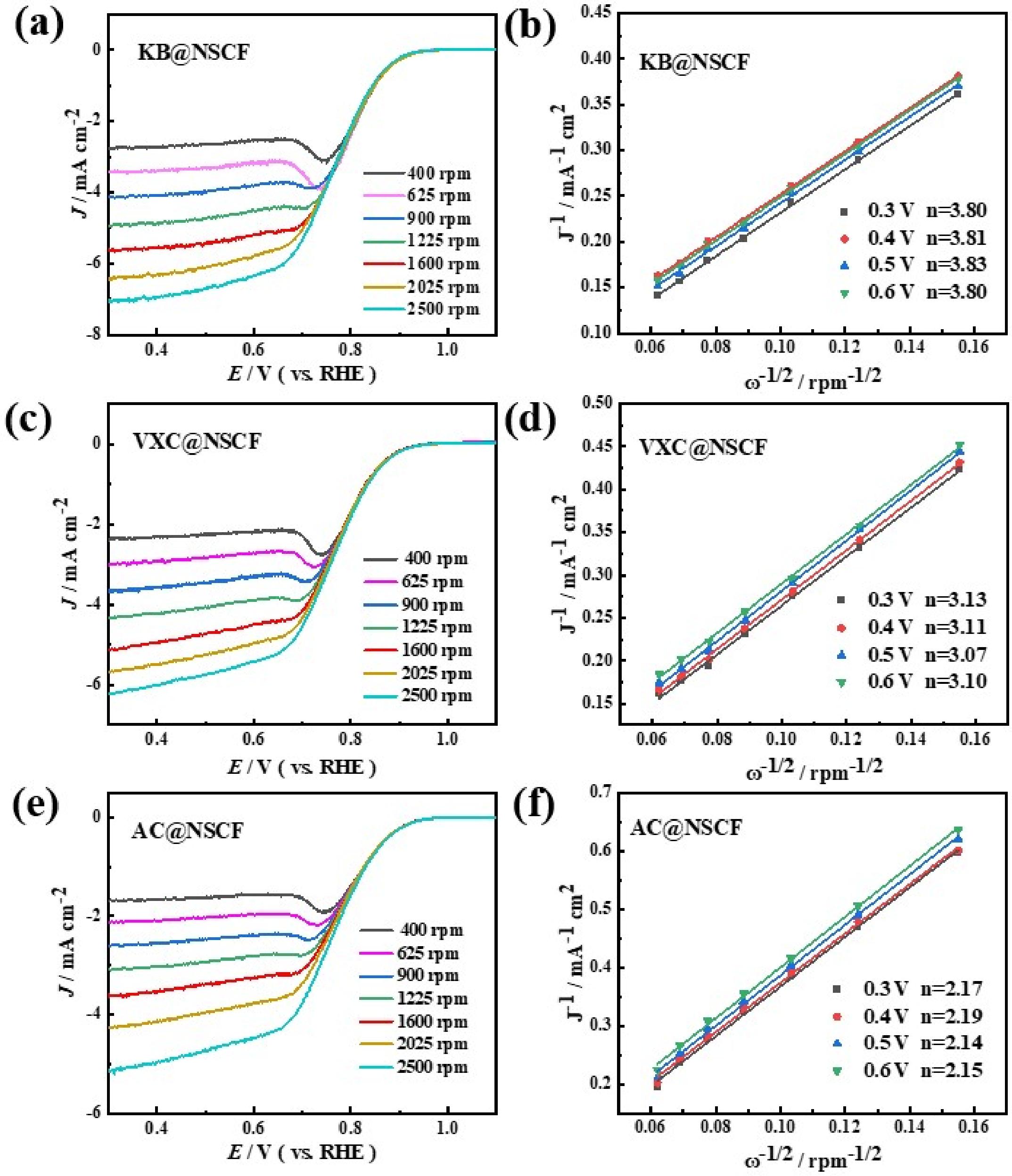

Figure S20. (a, c, e) ORR polarization curves of KB@NSCF, VXC@NSCF, and AC@NSCF recorded at different rotation speeds. (b, d, f) Linearly fitted K-L curves at different potential of KB@NSCF, VXC@NSCF, and AC@NSCF.

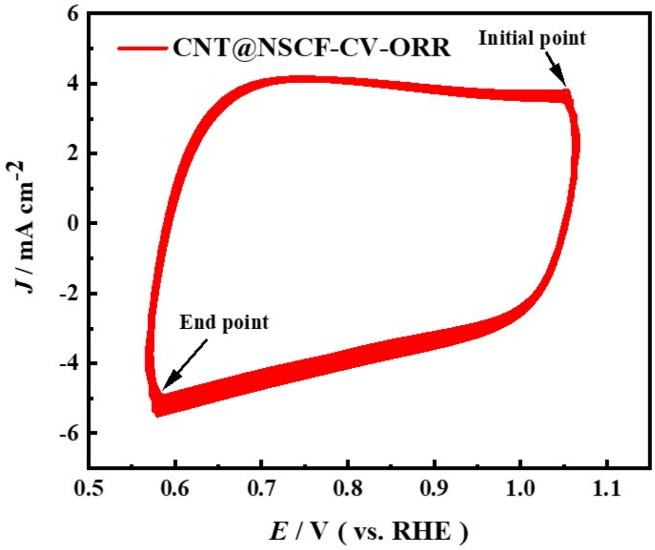

Figure S21. ORR cyclic measurements of CNT@NSCF at a scan rate of 100 mV s^{-1} for 8000 cycles.

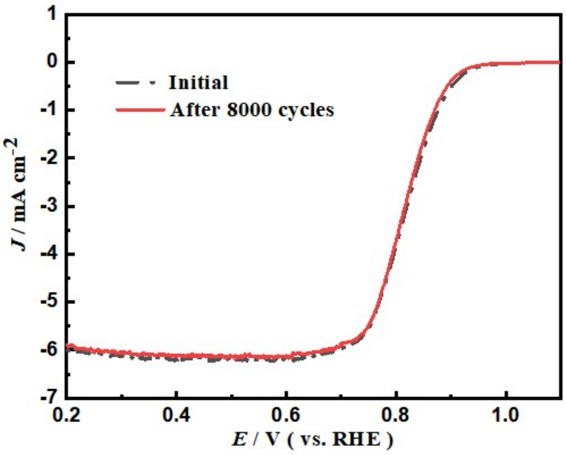

Figure S22. ORR curves of CNT@NSCF recorded at the first cycle and after 8000 cycles in an O_2-saturated 0.1 m KOH electrolyte.

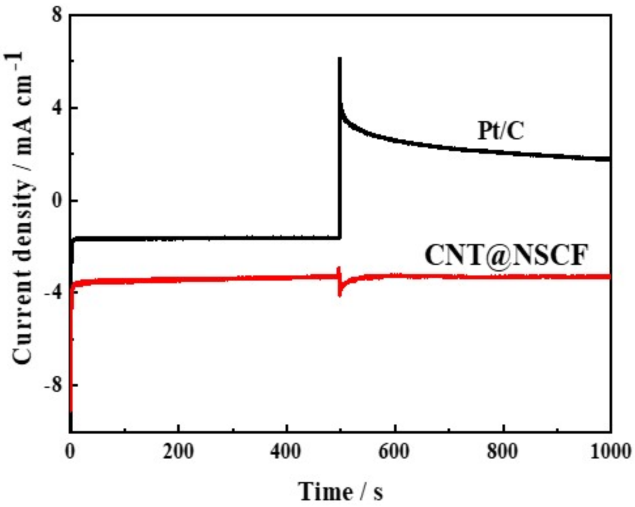

Figure S23. The methanol tolerance test of CNT@NSCF and Pt/C catalysts in an O_2-staurated 0.1 M KOH with 3.0 M CH_3OH.

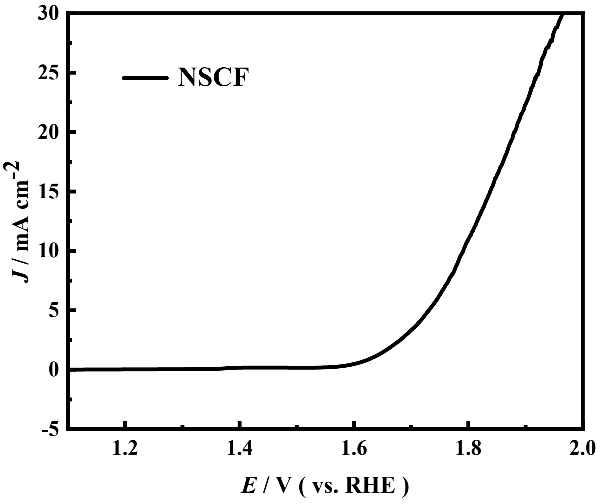

Figure S24. OER LSV curves of NSCF recorded at 1600 rpm and 10 mV s^{-1}.

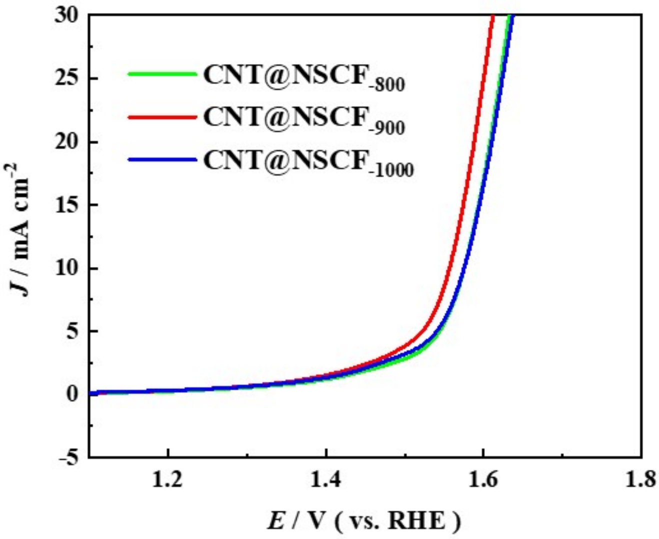

Figure S25. OER LSV curves of CNT@NSCF at different temperature recorded at 1600 rpm and 10 mV s^{-1}.

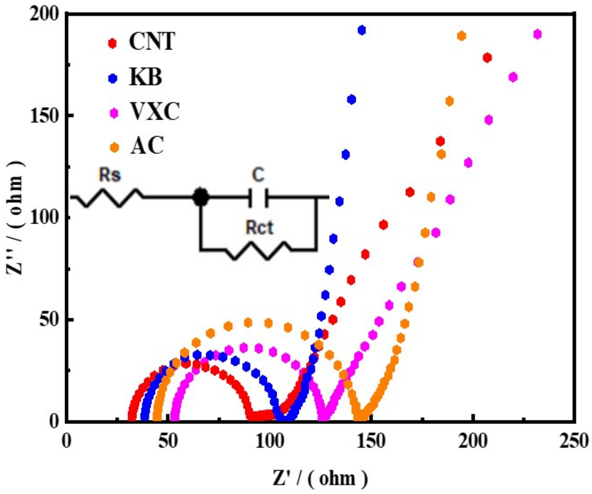

Figure S26. EIS Nyquist plots for the CNT, KB, VXC, and AC .

Table S6 The EIS fitting results (R_{ct}) of supports and catalysts.

catalysts	$\boldsymbol{R}_{\mathbf{ct}}$ / Ω	support	$\boldsymbol{R}_{\mathbf{ct}}$ / Ω	Δ$\boldsymbol{R}_{\mathbf{ct}}$ / Ω
CNT@NSCF	69.35	CNT	58.59	10.76
KB@NSCF	93.27	KB	66.85	26.42
VXC@NSCF	104.0	VXC	72.51	31.49
AC@NSCF	114.8	AC	98.85	15.95

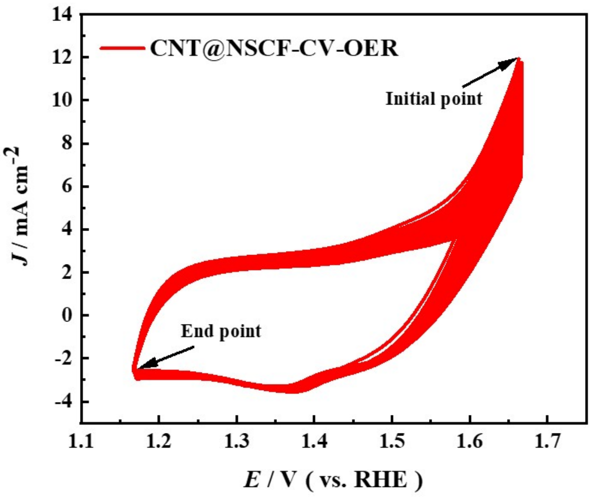

Figure S27. OER cyclic measurements of CNT@NSCF at a scan rate of 100 mV s^{-1} for 2000 cycles.

Table S7. The onset potential and half-wave potential of the ORR; the potential of OER at j=10 mA cm^{-2}; and the potential difference of CNT@NSCF, KB@NSCF, VXC@NSCF, AC@NSCF, NSCF, and Pt/C+RuO_2 in 0.1 M and 1 M KOH electrolyte.

Samples	E_{onset}/V	$E_{1/2}$ /V	$E_{j=10\ mA\ cm^{-2}}$/ V		$\Delta E=E_{j=10\ mA\ cm^{-2}} - E_{1/2}$ / mV	
			1 M	0.1 M	1 M	0.1 M
CNT@NSCF	0.94	0.82	1.56	1.67	740	850
KB@NSCF	0.90	0.79	1.58	1.69	790	900
VXC@NSCF	0.88	0.77	1.71	1.80	940	1030
AC@NSCF	0.89	0.79	1.73	1.81	940	1020
NSCF	0.84	0.73	1.78	1.87	1050	1140
Pt/C+RuO_2	0.98	0.84	1.59	1.69	750	850

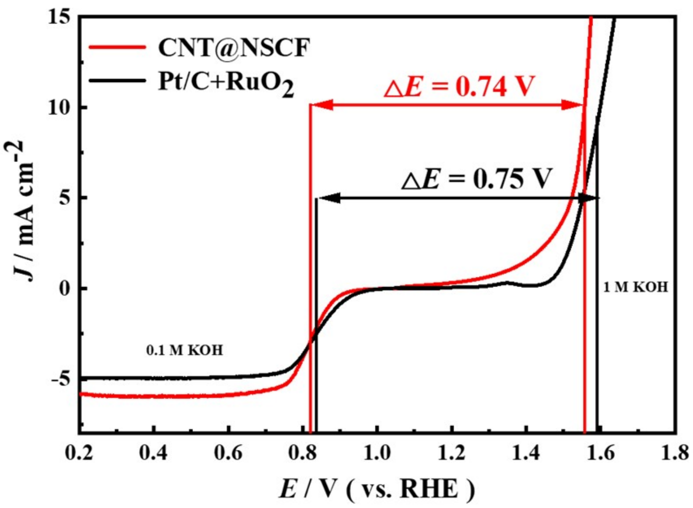

Figure S28. The overall polarization curves of CNT@NSCF, 20 wt. % Pt/C, and RuO_2 catalysts.

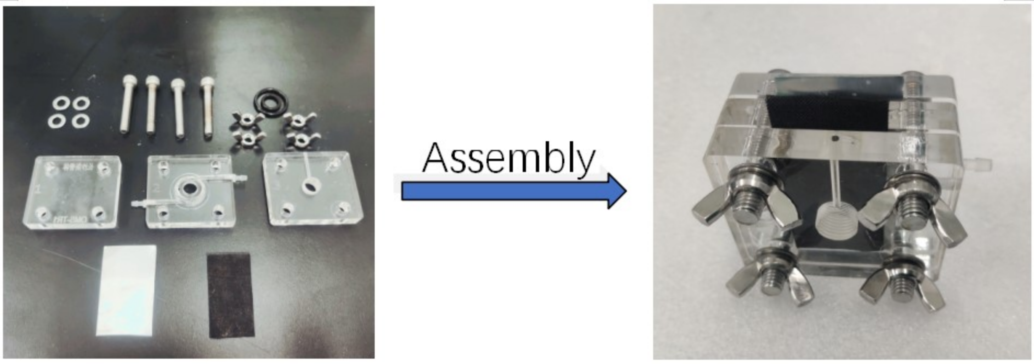

Figure S29. Assembly drawing of Zn-air battery.